



ELSEVIER

Coastal Engineering 36 (1999) 271–299

**COASTAL  
ENGINEERING**

www.elsevier.com/locate/coastaleng

# Generation of waves in Boussinesq models using a source function method

Ge Wei <sup>a,\*</sup>, James T. Kirby <sup>b</sup>, Amar Sinha <sup>a</sup>

<sup>a</sup> *CMS Consulting, Suite 219, 6797 North High Street, Worthington, OH 43085, USA*

<sup>b</sup> *Center for Applied Coastal Research, University of Delaware, Newark, DE 19716, USA*

Received 20 January 1998; received in revised form 11 November 1998; accepted 19 January 1999

---

## Abstract

A method for generating waves in Boussinesq-type wave models is described. The method employs a source term added to the governing equations, either in the form of a mass source in the continuity equation or an applied pressure forcing in the momentum equations. Assuming linearity, we derive a transfer function which relates source amplitude to surface wave characteristics. We then test the model for generation of desired incident waves, including regular and random waves, for both one and two dimensions. We also compare some model results with analytical solution and available experiment data. © 1999 Elsevier Science B.V. All rights reserved.

*Keywords:* Wave generation; Source function; Boundary condition; Boussinesq model

---

## 1. Introduction

The problem of generating and absorbing waves at the boundary of models based on Boussinesq-type equations is essentially an unsolved one, due to the fact that the exact structure of the well-posed initial boundary value problem is unknown for most forms of the model equations. Though it is possible to specify incident wave conditions at the wavemaker boundary, the characteristics of reflected waves in the computational domain cannot be determined a priori. One common approach is to assume the phase speed and the direction of reflected waves at the boundary, as proposed by Engquist and Majda

---

\* Corresponding author. Fax: +1-614-785-1414; E-mail: gwei@email.msn.com

(1977). Though the error from these approximate boundary conditions may be small at each time step of the simulation, the accumulated effect for long simulation times can be sufficiently large to cause the model to blow up. For instance, Wei and Kirby (1995) applied the approximate radiation condition at the wavemaker boundary in their extended Boussinesq model for simulating monochromatic wave propagation over an elliptic shoal. However, the simulation had to be terminated when sufficiently large reflected waves from the domain reached the wavemaker boundary. Though the general agreement between the model results from Engquist and Majda's method and experiment data is good, the source function method proposed below leads to significant improvements.

The sponge layer method proposed by Israeli and Orszag (1981) works quite effectively for dissipating waves with different phase speeds and directions. Models utilizing a sponge layer to implement a radiation condition can be run for fairly long simulation time without stability problems. However, in order to apply a sponge layer to absorb waves reflected toward the wavemaker, waves must be generated inside the computational domain instead of on the boundary. An example of this procedure is described by Larsen and Dancy (1983), who employ a line source to generate waves in a staggered-grid solution of Boussinesq-type equations. The method employed is somewhat ad hoc in that its performance is tuned to give good results for particular examples.

Line source methods are not well suited for use in all finite-difference realizations of Boussinesq equations. In particular, line source methods fail in the unstaggered-grid scheme described by Wei and Kirby (1995) for the extended Boussinesq equations of Nwogu (1993). For this reason, we develop here a source function method based on a spatially distributed source. The linearized form of the model equations including source terms can be solved using Green's functions, giving an explicit relation between the desired surface wave history and the source function history.

In Section 2, we describe the theoretical foundations of the source function method, considering both mass source terms used in the mass conservation equation, and applied pressure distributions used in the momentum equations. In Section 3, we show examples of generated monochromatic and random waves in both one and two dimensions. An analytical solution of the linearized equation with a finite source length for generating 2D monochromatic wave in a flat bathymetry is obtained and compared with model result. Comparisons are made between model results and experimental data for 1D random wave propagation over a constant slope (Mase and Kirby, 1992) and for 2D monochromatic wave propagation over a shoal geometry (Berkhoff et al., 1982). For 2D random waves, the reproduction of target wave spectra over constant water depth is demonstrated. In Section 4, we describe the use of the mass source term to control tidal effects during long model runs.

## 2. Theory

Here we consider the general problem of generating waves in a region oriented along the  $y$ -axis, as shown in the gray region in Fig. 1. It is assumed that  $x$  is the primary propagation direction for the waves. For an individual wave component,  $\theta$  is the angle

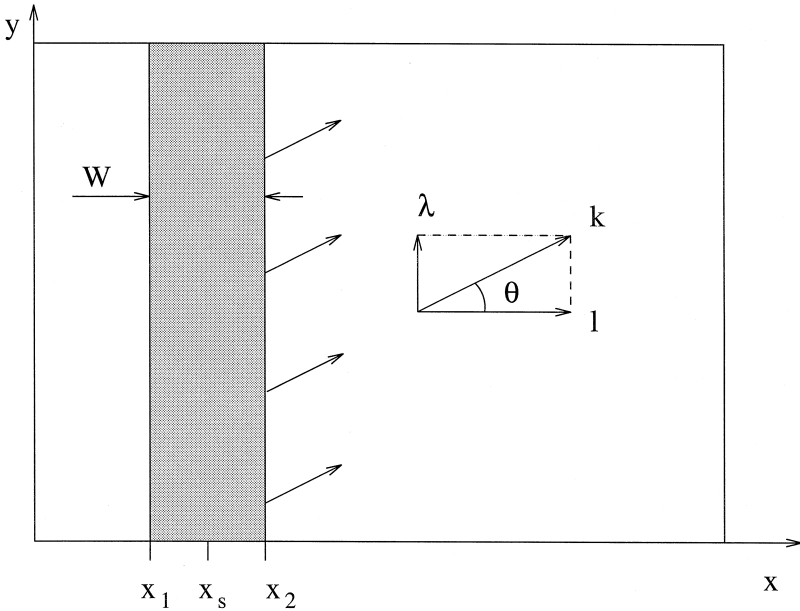


Fig. 1. Source function definition in computational domain.

between the propagation direction and  $x$ -axis. The forcing leading to wave generation is localized in some region  $x_1 \leq x \leq x_2$ , where  $|x_2 - x_1|$  will in general be a dimension on the order of a wavelength.

The wave generation mechanism considered here has been applied to the nonlinear long wave equations, the Boussinesq model based on depth-averaged velocity due to Peregrine (1967), and the Boussinesq model with extended dispersive effects due to Nwogu (1993), either in weakly nonlinear or fully nonlinear (Wei et al., 1995) form. In the following, we modify these equations by including either a scalar source term in the mass balance equation (thus mimicking a mass source) or a vector forcing term in the vector momentum equation (thus mimicking an applied scalar pressure distribution). In either case, we assume that the nonlinear effects will be small in the narrow source region. We linearize the governing equations to obtain an analytic solution in the source region. In the numerical implementation, nonlinearity is retained in the governing equations in the source region.

For waves in a horizontally 2D region of constant depth, the generalized form of the linearized Boussinesq and shallow water equations may be written as

$$\eta_t + h\nabla \cdot \mathbf{u} + \alpha_1 h^3 \nabla^2 (\nabla \cdot \mathbf{u}) = 0 \tag{1}$$

$$\mathbf{u}_t + g\nabla\eta + \alpha h^2 \nabla^2 \mathbf{u}_t = 0 \tag{2}$$

where  $h$  is the water depth,  $g$  is the gravitational acceleration,  $\eta$  is the surface elevation and  $\mathbf{u}$  is a velocity vector in the horizontal plane. The values of  $\alpha_1$  and  $\alpha$  have different definitions depending on the choice of equations. For the extended Boussinesq

equations of Nwogu (1993),  $\mathbf{u}$  is the velocity at the water depth  $z = z_\alpha$ , and  $\alpha_1 = \alpha + 1/3$ , with  $\alpha$  determined by:

$$\alpha = \frac{z_\alpha}{h} \left( \frac{1}{2} \frac{z_\alpha}{h} + 1 \right); \quad \frac{z_\alpha}{h} = -0.530 \tag{3}$$

For the Boussinesq equations of Peregrine (1967),  $\mathbf{u}$  is the depth-averaged velocity,  $\alpha_1 = 0$ , and  $\alpha = -1/3$ . For shallow water equations,  $\mathbf{u}$  is depth-averaged velocity and  $\alpha_1 = \alpha = 0$ .

Introducing a velocity potential  $\phi$ , we take  $\mathbf{u} = \nabla\phi$ . The model equations become

$$\eta_t + h\nabla^2\phi + \alpha_1 h^3 \nabla^2 \nabla^2 \phi = 0 \tag{4}$$

$$\phi_t + g\eta + \alpha h^2 \nabla^2 \phi_t = 0 \tag{5}$$

The linear dispersion relation for these equations may be obtained by considering a plane wave solution

$$\eta = \eta_0 \exp[i(kx - \omega t)]$$

$$\phi = \phi_0 \exp[i(kx - \omega t)]$$

and is given by

$$\omega^2 = gk^2 h \frac{1 - \alpha_1 (kh)^2}{1 - \alpha (kh)^2} \tag{6}$$

where  $\omega$  is the angular frequency and  $k$  the wavenumber. The relation between the amplitude of the velocity potential  $\phi_0$  and the wave amplitude  $\eta_0$  is given by

$$\eta_0 = \frac{i\omega}{g} [1 - \alpha (kh)^2] \phi_0. \tag{7}$$

### 2.1. Source function in continuity equation

We first add a source function  $f(x, y, t)$  to Eq. (1) and find the corresponding solution of the following equations

$$\eta_t + h\nabla \cdot \mathbf{u} + \alpha_1 h^3 \nabla^2 (\nabla \cdot \mathbf{u}) = f(x, y, t) \tag{8}$$

$$\mathbf{u}_t + g\nabla\eta + \alpha h^2 \nabla^2 \mathbf{u}_t = 0 \tag{9}$$

We introduce a velocity potential  $\phi$ , integrate Eq. (9) once, and eliminate  $\eta$  in favor of  $\phi$  to obtain the equation

$$\phi_{tt} - gh\nabla^2\phi + \alpha h^2 \nabla^2 \phi_{tt} - \alpha_1 gh^3 \nabla^2 \nabla^2 \phi = -gf(x, y, t). \tag{10}$$

We now assume that the  $y$  and  $t$  dependence of  $\phi$  and  $f$  is suitable for a Fourier transform and introduce

$$\phi(x, y, t) = \frac{1}{4\pi^2} \int_{-\infty}^{\infty} \int_{-\infty}^{\infty} \hat{\phi}(x, \lambda, \omega) \exp(i\lambda y - i\omega t) d\lambda d\omega \tag{11}$$

$$f(x, y, t) = \frac{1}{4\pi^2} \int_{-\infty}^{\infty} \int_{-\infty}^{\infty} \hat{f}(x, \lambda, \omega) \exp(i\lambda y - i\omega t) d\lambda d\omega \tag{12}$$

where  $\lambda = k \sin(\theta)$  is the wavenumber in  $y$  direction,  $\omega$  is the angular frequency of the wave. Substituting Eqs. (11) and (12) into Eq. (10) results in a fourth order ordinary differential equation (ODE) for  $\hat{\phi}$  with respect to  $x$

$$A\hat{\phi}^{(4)} + B\hat{\phi}'' + C\hat{\phi} = g\hat{f} \tag{13}$$

where

$$\begin{aligned} A &= \alpha_1 gh^3 \\ B &= gh + \alpha\omega^2 h^2 - 2\alpha_1 gh^3\lambda^2 \\ C &= \omega^2 - gh\lambda^2 - \alpha\omega^2 h^2\lambda^2 + \alpha_1 gh^3\lambda^4 \end{aligned} \tag{14}$$

This equation reduces to a second-order equation for either the long wave or Peregrine models, where  $A = 0$ . Homogeneous solutions of Eq. (13) corresponding to progressive waves are given by

$$\hat{\phi}_h(x) = \exp(\pm ilx) \tag{15}$$

where  $l = \sqrt{k^2 - \lambda^2} = k \cos(\theta)$  is the wavenumber in the  $x$  direction. In order to obtain the particular solution for  $\hat{\phi}$ , we seek a Green's function  $G(x, x')$  which satisfies

$$AG^{(4)} + BG'' + CG = \delta(x - x') \tag{16}$$

We impose the boundary conditions on the Green's function to correspond to the condition that waves are radiating away from the source region (where superscript  $n$  inside parenthesis denotes the order of differentiation)

$$\begin{aligned} G^{(n)} &\rightarrow (+il)^n G, & \hat{\phi}^{(n)} &\rightarrow (+il)^n \hat{\phi}; & x &\rightarrow +\infty \\ G^{(n)} &\rightarrow (-il)^n G, & \hat{\phi}^{(n)} &\rightarrow (-il)^n \hat{\phi}; & x &\rightarrow -\infty \end{aligned} \tag{17}$$

Integrating Eq. (16) with respect to  $x$  from  $x' - 0$  to  $x' + 0$ , we have

$$AG'''(x, x')|_{x=x'-0}^{x=x'+0} + BG'(x, x')|_{x=x'-0}^{x=x'+0} + C \int_{x'-0}^{x'+0} G(x, x') dx = 1. \tag{18}$$

The solution for the Green's function takes different forms depending on the value of  $A$ .

### 2.1.1. Case 1: $A = 0$

If  $A = 0$  ( $\alpha_1 = 0$ , i.e., corresponding to standard Boussinesq equations or nonlinear shallow water equations), Eq. (18) becomes

$$BG'(x, x')|_{x=x'-0}^{x=x'+0} + C \int_{x'-0}^{x'+0} G(x, x') dx = 1. \tag{19}$$

In addition to boundary conditions (17), we require  $G$  to be continuous at  $x = x'$ . Eq. (19) then reduces to

$$BG'(x, x')|_{x=x'-0}^{x=x'+0} = 1. \tag{20}$$

The Green’s function is given by

$$G(x, x') = \begin{cases} a \exp[il(x - x')] & \text{if } x > x' \\ a \exp[il(x' - x)] & \text{if } x < x' \end{cases} \tag{21}$$

which automatically satisfies the boundary conditions (17) and is continuous at  $x = x'$ . Substituting Eq. (21) into Eq. (20) results in

$$a = -\frac{i}{2lB} = \frac{il}{\omega^2}. \tag{22}$$

As will be shown below, the above relation is included in the next case by specifying  $\alpha_1 = 0$ .

*2.1.2. Case 2: A ≠ 0*

For  $A \neq 0$  ( $\alpha = -0.39$ ,  $A < 0$ , i.e., corresponding to the case of extended Boussinesq equations), we require that  $G$ ,  $G'$ ,  $G''$  are continuous at  $x = x'$ . Thus the second and third terms in Eq. (18) drop out and we have

$$AG'''(x, x')|_{x=x'+0}^{x=x'-0} = 1. \tag{23}$$

The Green’s function is given by

$$\begin{aligned} G(x, x') &= a \exp[il_1(x - x')] + b \exp[il_2(x - x')] & \text{if } x > x' \\ G(x, x') &= a \exp[il_1(x' - x)] + b \exp[il_2(x' - x)] & \text{if } x < x' \end{aligned} \tag{24}$$

where  $l_1 = l = k \cos(\theta)$  and  $l_2 = iL$  ( $L > 0$ ) are the real and imaginary wavenumbers which satisfy the homogeneous form of Eq. (13). The Green’s function  $G$  in Eq. (24) automatically satisfies the boundary conditions (17). In addition,  $G$  and  $G''$  are continuous at  $x = x'$ . The continuity requirement of  $G'$  at  $x = x'$  results in

$$l_1 a + l_2 b = 0. \tag{25}$$

Substituting Eq. (24) into Eq. (23) gives

$$-2Ai(l_1^3 a + l_2^3 b) = 1. \tag{26}$$

From Eqs. (25) and (26), we obtain

$$a = \frac{i}{2Al_1(l_1^2 - l_2^2)}. \tag{27}$$

Using linear dispersion relation (6) and definitions of  $l_1$  and  $l_2$ , we can express  $a$  as

$$a = -\frac{ik}{2(\omega^2 - \alpha_1 gk^4 h^3) \cos \theta}. \tag{28}$$

Terms associated with  $b$  in Green’s function  $G(x, x')$  correspond to the evanescent mode and is negligible for large  $|x - x'|$ .

**2.1.3. Solution and choice of source function  $f$**

Now we seek the solution for  $\hat{\phi}$  by using the Green’s function  $G$ . Multiplying Eq. (16) by  $\hat{\phi}(x')$  and integrating with respect to  $x'$  from  $-\infty$  to  $+\infty$  gives

$$\int_{-\infty}^{+\infty} \hat{\phi}(x') \left[ AG(x, x')^{(4)} + BG(x, x')'' + CG(x, x') \right] dx' = \int_{-\infty}^{+\infty} \hat{\phi}(x') \delta(x - x') dx' \tag{29}$$

Integration by parts, use of the boundary conditions (17), and use of the definition of the delta function then gives

$$\hat{\phi}(x) = \int_{-\infty}^{+\infty} G(x, x') g\hat{f}(x') dx' = \int_{-\infty}^x G_+(x, x') g\hat{f}(x') dx' + \int_x^{+\infty} G_-(x, x') g\hat{f}(x') dx'. \tag{30}$$

In principle, the source function  $\hat{f}$  can be of any shape. For the examples that follow, we have adopted a smooth Gaussian shape for  $\hat{f}$  as

$$\hat{f}(x) = D \exp(-\beta x^2) \tag{31}$$

where  $D$  is the source function amplitude to be determined later from the desired wave characteristics, and  $\beta$  is a parameter associated with the width of source function. The definition (31) keeps the source function fairly well localized, i.e., for sufficiently large value of  $x$  (or away from source region, say  $\beta x^2 > 5$ ) the source function  $\hat{f}(x)$  is negligibly small. The second integral in the right hand side of Eq. (30) can be dropped and thus we have

$$\hat{\phi}(x) = \int_{-\infty}^x G_+(x, x') g\hat{f}(x') dx' \simeq gD [aI_1 \exp(ilx) + bI_2 \exp(-Lx)] \tag{32}$$

where  $I_1$  and  $I_2$  are defined by

$$I_1 = \int_{-\infty}^{\infty} \exp(-\beta x'^2) \exp(-ilx') dx' = \sqrt{\frac{\pi}{\beta}} \exp\left(-\frac{l^2}{4\beta}\right) \tag{33}$$

$$I_2 = \int_{-\infty}^{\infty} \exp(-\beta x'^2) \exp(Lx') dx' = \sqrt{\frac{\pi}{\beta}} \exp\left(\frac{L^2}{4\beta}\right). \tag{34}$$

Since  $L > 0$ , the last term in Eq. (32) is exponentially decayed and its contribution is negligible for sufficiently large  $x$ . Therefore, the corresponding velocity potential becomes

$$\hat{\phi}(x) = gDaI_1 \exp(ilx) = \phi_0 \exp(ilx). \tag{35}$$

Using relation (7) and expression (28), we finally have

$$D = \frac{2\eta_0(\omega^2 - \alpha_1 g k^4 h^3) \cos \theta}{\omega I_1 k [1 - \alpha(kh)^2]}. \quad (36)$$

In summary, for given wave frequency  $\omega$ , wave direction  $\theta$  (or  $\lambda$ ), wave amplitude  $\eta_0$ , water depth  $h$ , and source width parameter  $\beta$ , the corresponding source amplitude  $D$  can be determined from the above formula.

## 2.2. Source function in the momentum equation

Alternately, we can add a source term in the vector momentum equation according to

$$\mathbf{u}_t + g\nabla\eta + \alpha h^2 \nabla^2 \mathbf{u}_t = -g\nabla P \quad (37)$$

where  $P$  is a normalized pressure distribution having units of length. Using the velocity potential, Eq. (37) may be integrated to give

$$\phi_t + g\eta + \alpha h^2 \nabla^2 \phi_t = P. \quad (38)$$

Combining the continuity and momentum equations then gives

$$\phi_{tt} - gh\nabla^2 \phi + \alpha h^2 \nabla^2 \phi_{tt} - \alpha_1 gh^3 \nabla^2 \nabla^2 \phi = -P_t. \quad (39)$$

Comparing Eqs. (39) and (10) gives

$$P = g \int f dt. \quad (40)$$

Introducing the Fourier transform for  $P$ ,

$$P = \frac{1}{4\pi^2} \int \int \hat{P} \exp[i(\lambda y - \omega t)] d\lambda d\omega, \quad (41)$$

we obtain

$$\hat{P} = \frac{ig}{\omega} \hat{f}. \quad (42)$$

The remainder of the solution for this case follows similarly from Section 2.1.

## 3. Model tests

In this section, we use the source function method to study several cases of wave generation and propagation, for both monochromatic and random waves. All examples in this section are computed using the source function  $f(x, y, t)$  in the mass conservation equation.

As mentioned in Section 2, the source function amplitude  $D$  is not only a function of the desired wave characteristics, but also a function of  $\beta$ , the free parameter describing the source width. The area inside the source region is essentially wasted space since waves there are not the same as target waves generating to the far field. A large  $\beta$  value

is generally preferred since the corresponding source region is narrower, equivalent to enlarge the effective computing domain. However, too large value of  $\beta$  may result in a poor finite difference representation of the source region. For the source function described by Eq. (31), we define the width as

$$W = |x_2 - x_1| \quad (43)$$

where  $x_1$  and  $x_2$  are the roots of the equation

$$\exp[-\beta(x - x_s)^2] = \exp(-5) = 0.0067 \quad (44)$$

From Eqs. (43) and (44), we have

$$W = 2\sqrt{5/\beta}. \quad (45)$$

The source function width  $W$  can also be related to the wavelength  $L$  as

$$W = \delta(L/2). \quad (46)$$

Eliminating  $W$  from Eqs. (45) and (46), we have

$$\beta = \frac{80}{\delta^2 L^2}. \quad (47)$$

The typical value of  $\delta$  we use in the model is in the range of 0.3–0.5 and the corresponding source function width is about 0.15–0.25 times the wavelength. For random wave generation, however, we choose a representative wave (e.g., with peak frequency and in main propagation direction) to determine a fixed  $\beta$  for all wave components, i.e.,

$$\hat{f}(x, \lambda, \omega) = D(\lambda, \omega) \exp(-\beta x^2) \quad (48)$$

where  $D$  is the amplitude of each spectral component. Then the resulting source function can be written as

$$\begin{aligned} f(x, y, t) &= \frac{1}{4\pi^2} \iint D(\lambda, \omega) \exp(-\beta x^2) \exp[i(\lambda y - \omega t)] d\omega d\lambda \\ &= \exp(-\beta x^2) F(y, t) \end{aligned} \quad (49)$$

which results in significant saving on computing time for random wave simulation.

### 3.1. 1D monochromatic wave

To verify the source function method, we apply the model to generate 1D monochromatic waves over a domain with constant water depth. The extended Boussinesq equations of Nwogu (original and linearized) are used in the model.

#### 3.1.1. Wave generation

We consider a computational domain shown in Fig. 2. The horizontal length of the domain is  $L_x = 50$  m and the water depth  $h = 0.5$  m is constant. The center of the source region is located at  $x_s = 25$  m. To absorb wave energy, two sponge layers of 5 m width are placed at both ends of the domain. The properties of these sponge layers are the same as those described by Wei and Kirby (1995).

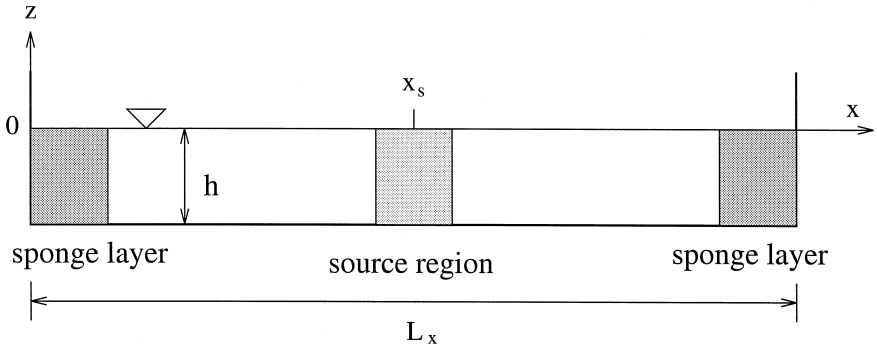


Fig. 2. The computational domain used to illustrate the source function method for generating 1D monochromatic wave.

We are going to generate a monochromatic wave with period  $T = 1$  s (the corresponding wavelength is about 1.5 m) and height  $H = 0.05$  m, which is in the range of waves generated by many laboratory experiments. The grid size used in the model is  $\Delta x = 0.02$  m and the time step is  $\Delta t = 0.02$  s. The coefficient related to source function width in Eq. (47) is specified as  $\delta = 0.3$ , making the source region width about 19 grid points. We run the model up to 100 s of simulation without encountering any stability problems. Fig. 3 shows the snapshots of surface elevation  $\eta$  at various time ( $t/T = 10, 20, 40, 100$ ).

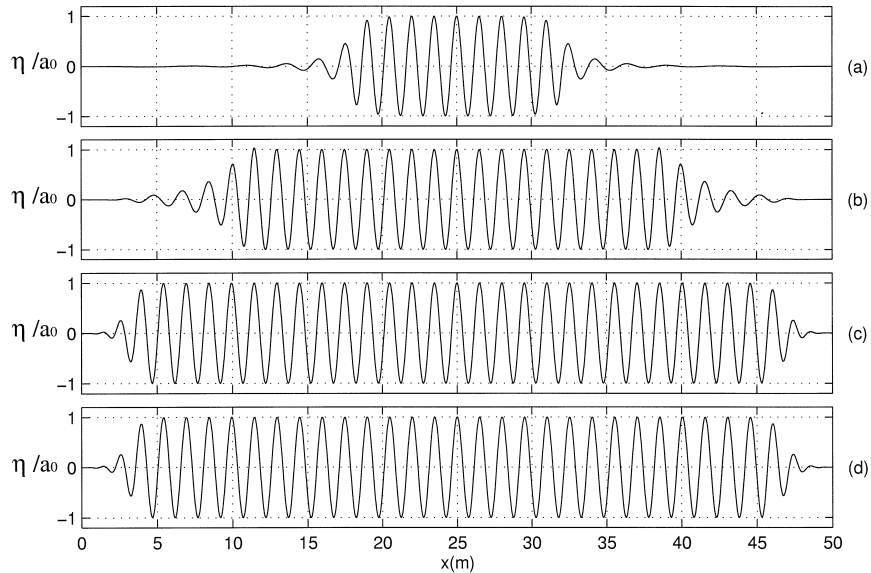


Fig. 3. Snapshots of surface elevation at different times: (a)  $t/T = 10$ ; (b)  $t/T = 20$ ; (c)  $t/T = 40$ ; (d)  $t/T = 100$ .

We see that waves are generated first at the source region at the center of the domain and then propagate towards the two ends. Sponge layers at both ends of the domain work quite well to dissipate wave energy, as evident by the decreasing wave height over sponge layer region. The wave fields at  $t/T = 40$  and at  $t/T = 100$  are almost identical, indicating that quasi-steady state is reached at  $t/T = 40$ . The wave crests and troughs at these time are very close to the dashed grid lines, which are also the height of the target wave. Further quantitative analysis shows that the relative error between the target and generated wave height is less than 0.2%.

### 3.1.2. Waves with different periods

Next we apply the model to generate monochromatic waves with four different periods  $T = (0.5, 1.5, 2.0)$  s. All model parameters (e.g., water depth, domain length, grid size, time step, and source function width) are kept the same as those in the previous example for  $T = 1$  s. We run the model up to  $t = 100$  s for all these waves and there was no stability problem. Fig. 4 shows the snapshots of surface elevations at  $t = 100$  s for all four waves with periods  $T = (0.5, 1.0, 1.5, 2.0)$  s.

The generated wave fields shown in Fig. 4 are quite good and the corresponding wave heights are very close to their target value. Since all the model parameters except for input wave period are kept the same, the corresponding numbers of grid points per wavelength or the numbers of time step per wave period are different for each wave. For instance, there are about 24 grid points per wavelength for the case of  $T = 0.5$  s and about 194 grid points per wavelength for  $T = 2.0$  s. These results indicate that the model can be applied to simulate random waves which consist of superposed monochromatic wave components with different frequencies and directions.

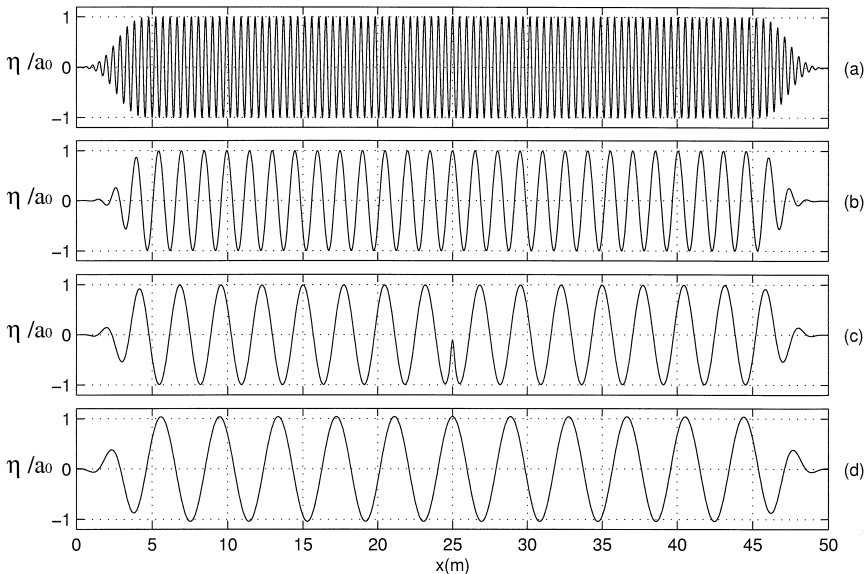


Fig. 4. Snapshots of surface elevation at  $t = 100$  s: (a)  $T = 0.5$  s; (b)  $T = 1.0$  s; (c)  $T = 1.5$  s; and (d)  $T = 2.0$  s.

### 3.1.3. Waves with different amplitudes

The two previous tests are based on the linearized form of Nwogu’s extended Boussinesq equations. Except for numerical error, model results should match those derived from the source function theory in Section 2. In real application, however, the original nonlinear model must be used to obtain useful information of wave transformation. We therefore run the nonlinear model to generate waves with various amplitudes.

The snapshots of surface elevation at  $t/T = 100$  for different wave amplitudes ( $H/h = 0.1, 0.2, 0.3$ ) are shown in Fig. 5. For comparison, the snapshot obtained from linearized model for  $H/h = 0.1$  is also included. In Fig. 5(a), wave crests and troughs are on the lines of  $\eta/a_0 = \pm 1$ . The shapes of crests and troughs are symmetric both horizontally and vertically, indicating that the generated waves are linear. In Fig. 5(b)–(c), however, wave shapes are no longer symmetric. Wave crests are over the line of  $\eta/a_0 = 1$  and wave troughs do not reach the line  $\eta/a_0 = -1$ . Further analysis shows that the wave crests are sharp and wave troughs are flat, indicating that nonlinear waves are generated. As wave amplitude increases, the asymmetry between crests and troughs becomes larger.

### 3.1.4. Wave reflection and absorption

In all previous tests, there is no wave reflection due to constant water depth and wave energy absorption by sponge layers at both ends of the domain. Now we change the domain physics to illustrate the capability of the model for handling reflecting waves. The original Nwogu’s equations are used for this case.

We take out the sponge layer at the right end in Fig. 2 and move the source to  $x_s = 24.4$  m. The boundary at the right end will be reflecting wall. Except for smaller

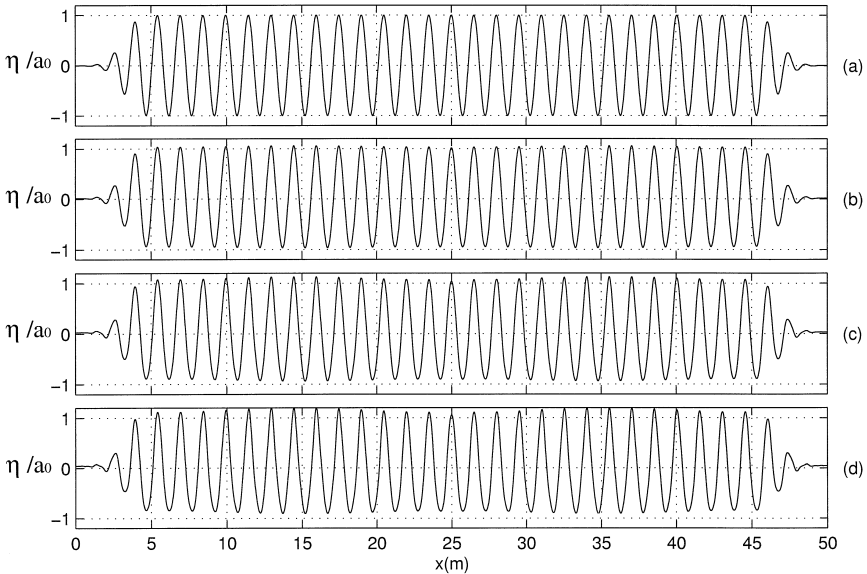


Fig. 5. Snapshots of surface elevation at  $t/T = 100$ : (a)  $H/h = 0.1$  (linear); (b)  $H/h = 0.1$ ; (c)  $H/h = 0.2$ ; and (d)  $H/h = 0.3$ .

time step ( $\Delta t = 0.01$  s) and longer simulation time (up to 200 s), all model parameters are the same as previous cases. Fig. 6 shows the corresponding results. In each plot of Fig. 6, we superpose four snapshots of surface elevation with  $T/4$  interval, i.e., at  $t = t_i$ ,  $t = t_i + T/4$ ,  $t = t_i + T/2$ , and  $t = t_i + 3T/4$ , where  $t_i = 40$  s, 80 s, 120 s, 200 s for (a), (b), (c) and (d), respectively. In the early stage, waves are generated from the source region and propagate to both ends. Waves are then absorbed at the left end by sponge layer but are reflected once they reach the wall at the right end. There exist three wave trains in the domain, the first propagates to the left from the source region, the second propagates to the right from the source region, and the third propagates to the left from the reflecting wall. The resulting wave field will be standing waves on the right side of the source and progressive waves on the left side, as shown in the corresponding plots (b), (c) and (d).

Notice that the amplitude of the progressive waves is about twice the initial value. This is due to the fact that the distance of the source to the wall is 26.60 m, equivalent to 17 wavelengths, resulting in the same phase for the generated waves by the source and the reflecting waves from the wall. It is evident that the sponge layer on the left is capable of absorbing the waves generated by the source as well as the reflecting waves from the wall.

### 3.2. 1D random wave

Mase and Kirby (1992) conducted a laboratory study of random wave propagation over a slope. The layout of the experiment is shown in Fig. 7, where a constant water

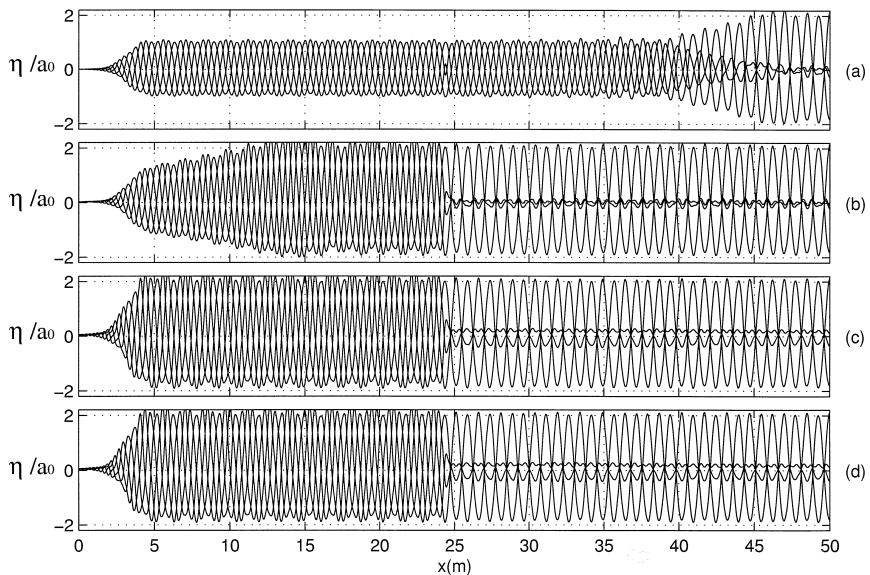


Fig. 6. Superposition of four snapshots for surface elevation at  $t_i$ ,  $t_i + T/4$ ,  $t_i + T/2$ ,  $t_i + 3T/4$ : (a)  $t_i = 40$  s; (b)  $t_i = 80$  s; (c)  $t_i = 120$  s; (d)  $t_i = 200$  s.

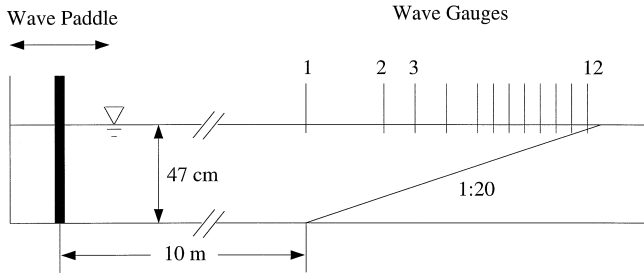


Fig. 7. Experiment layout of Mase and Kirby (1992).

depth 0.47 m on the left connects to a constant slope (1/35) on the right. Based on Pierson–Moskowitz spectrum, two sets of random waves with peak frequencies 0.6 Hz (referred to as run 1) and 1.0 Hz (run 2) are generated by the wavemaker on the left end and propagate to the right end. Starting at the toe of the slope, 12 wave gauges are deployed along the slope at the various locations. Time series of surface elevation at these gauges are collected simultaneously for about 15 min for run 1 and about 13 min for run 2.

We now apply the model to simulate the experiment of Mase and Kirby (1992) for case run 2. The model equations used here are the fully nonlinear Boussinesq equations of Wei et al. (1995). Eddy viscosity terms (Wei, 1997) are included in the equations to dissipate wave energy due to wave breaking. To generate the corresponding random wave field from the experiment data, we express the time series of surface elevation  $\eta(t)$  and the time series of source function  $F(t)$  as

$$\eta(t) = \frac{1}{2\pi} \int \eta_0(\omega) \exp(-i\omega t) d\omega \tag{50}$$

$$F(t) = \frac{1}{2\pi} \int D(\omega) \exp(-i\omega t) d\omega \tag{51}$$

Using the time series data of surface elevation  $\eta(t)$  at the first wave gauge on the toe, we first obtain the corresponding Fourier coefficients  $\eta_0(\omega)$  by FFT method. Applying expression (36), the Fourier coefficients of source function  $D(\omega)$  for each component are then determined. Applying an inverse FFT, we then obtain the corresponding time series of source function  $F(t)$ , which serves as the input for the model.

The grid size for the model is  $\Delta x = 0.025$  m and the time step is  $\Delta t = 0.02$  s. The shoreline condition on the right end in the experiment is replaced by a constant water depth of 2.0 cm with sponge layer in the model. The wavemaker in the model is located at the toe of the slope, where experimental data is available. Fig. 8 shows a comparison of time series of surface elevation from  $t = 20$  s to  $t = 40$  s at different gauge locations. Except for some phase differences in a few shallow water gauges, the agreement between the model results and the experimental data is quite good for both wave height and phase.

The discrepancy between the model and data for wave phase in shallow water regions may be due to the replacement of the shoreline boundary condition by a constant depth

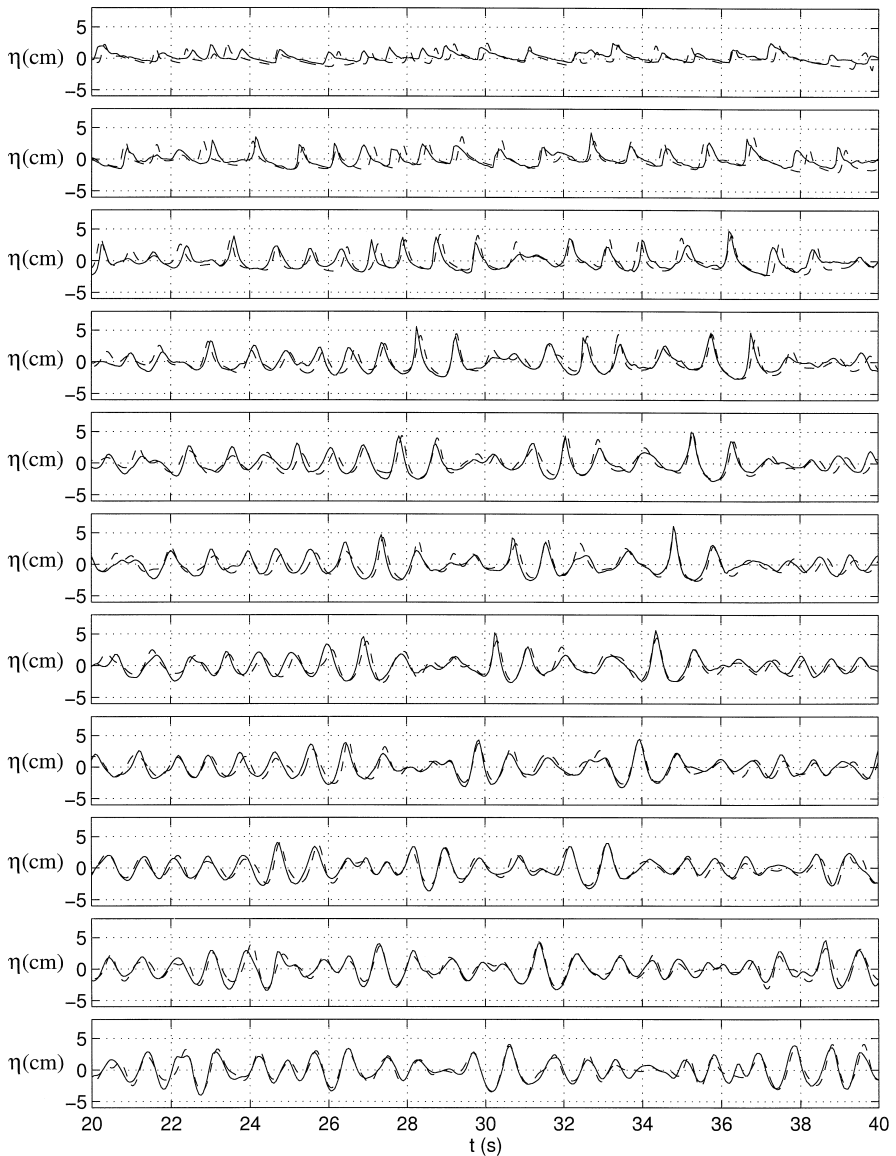


Fig. 8. Comparison of surface elevation between model (---) and data (—) at various gauge locations: (a)  $h = 2.5$  cm; (b)  $h = 5$  cm; (c)  $h = 7.5$  cm; (d)  $h = 10$  cm; (e)  $h = 12.5$  cm; (f)  $h = 15$  cm; (g)  $h = 17.5$  cm; (h)  $h = 20$  cm; (i)  $h = 25$  cm; (j)  $h = 30$  cm; (k)  $h = 35$  cm.

of sponge layer in the model. Wave reflection at the shoreline is different from that from the sponge layer. Work has been done to include a shoreline boundary condition in the model, and it is expected that the comparison between the model and data at shallow water gauges will be improved in future versions of the model.

We run the model for the entire length of experimental data. The agreement of time series for surface elevation at other intervals between the model and data is similar to that in Fig. 8. From the time series data, we evaluate the corresponding statistical properties such as standard deviation, skewness, and asymmetry. Since we start the model from zero initial condition, the beginning portion of model data (about 20 s) has to be discarded for comparison with experimental data. Fig. 9 shows the comparison of standard deviation and third moment statistics (skewness and asymmetry) between the model and data.

These statistical quantities are important measurements for a random wave train. The standard deviation is proportional to the root mean square wave height, or the energy of the wave train. The skewness and asymmetry give quantitative measurement for the degree of change of a wave shape from the sinusoidal function. These quantities are also

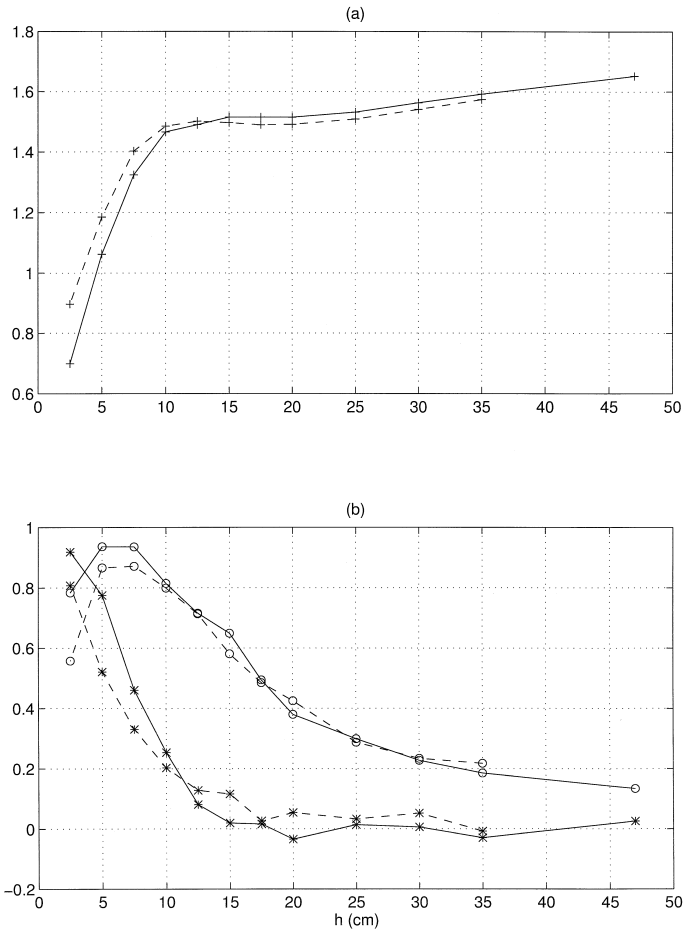


Fig. 9. Comparison of statistical properties between model (---) and data (—) at various gauge locations: (a) standard deviation; (b) skewness (◊) and asymmetry (\*).

important for calculating forcing in sediment transport. The close agreement between the model and data indicates that the source function method works well.

### 3.3. 2D monochromatic wave

The situation for 2D wave generation is quite different from that in 1D case. As shown in Eq. (36), the source function amplitude is related to  $\theta$ , the angle between the  $x$ -axis and the propagation direction of target wave. For the same wave with different propagation directions, their corresponding source function amplitudes  $D$  are different. In addition, the source function  $f(x, y, t)$  will be a function of  $y$ .

Another important factor to be considered in 2D wave generation is the effect of diffraction. The derivation in Section 2 is based on the assumption of infinite source length in  $y$  direction, which is not possible for any practical models whose domain size must be finite. For this reason, the generated wave field close to the boundary and far away from source region will not be as strictly uniform as shown in the derivation. This situation is similar to the wave field behind a breakwater gap. The uniformity of the wave field is proportional to the gap size (or source length in the model).

In the following, we will show two examples of 2D monochromatic wave generation and propagation. We first run the model over a domain of constant water depth with a finite length source region. Analytical solution for this case is available and will be compared with model results. We then apply the model to study the experiment of Berkhoff et al. (1982) for wave propagation over a complex geometry. Comparisons are made between model results and experiment data for wave amplitudes along eight transects in the domain.

#### 3.3.1. Comparison to analytical solution

The Helmholtz equation is the linear and exact governing equation for wave propagation over different water depth. For the special case of constant water depth and infinite domain, there exists analytical solution for finite length of source region (Greenberg, 1971). The Helmholtz equation in constant water depth  $h$  for the complex variable of surface elevation  $\eta(x, y)$  is given by

$$\eta_{xx} + \eta_{yy} + k^2\eta = 0 \quad (52)$$

where subscripts denote partial derivatives with respect to  $x$  and  $y$ , and  $k$  is the wavenumber which is determined from the linear dispersion relation  $\omega^2 = gk \tanh(kh)$ .

For an infinite domain with a point source located at  $(x', y')$ , the solution of the corresponding wave field at any point  $(x, y)$  is given by

$$\eta(x, y) = A [J_0(kr) + iY_0(kr)] \quad (53)$$

where  $A$  is a constant to be determined from the boundary condition (e.g., wave height and phase at a specific point),  $J_0$  and  $Y_0$  are first and second kinds of Bessel function of zero order,  $i$  is the unit imaginary number, and  $r$  is the distance between point  $(x, y)$  and point  $(x', y')$ , which is defined as

$$r = \sqrt{(x - x')^2 + (y - y')^2}. \quad (54)$$

For a source region with finite dimension as that used in the numerical model (i.e.,  $x_1 < x < x_2$ ,  $y_1 < y < y_2$ ), the corresponding solution is

$$\eta(x, y) = A \int_{y_1}^{y_2} \int_{x_1}^{x_2} f(x', y') [J_0(kr) + iY_0(kr)] dx' dy' \tag{55}$$

where  $A$  is a constant to be determined from desired wave condition,  $f(x', y')$  is the variation of the desired wave in the source region. In order to compare the analytical solution with the numerical model, we define

$$f(x', y') = \begin{cases} \exp[-\beta(x' - x_s)^2 + i(lx' + \lambda y' + \xi)], & x_1 < x' < x_2, y_1 < y' < y_2; \\ 0, & \text{otherwise} \end{cases} \tag{56}$$

where  $x_s$  is the center source line location,  $\beta$  is the width parameter of source function determined by Eq. (47) from the numerical model,  $x_1$ ,  $x_2$ ,  $y_1$  and  $y_2$  are the boundary coordinate of the source region,  $l$  and  $\lambda$  are the wavenumbers in  $x$  and  $y$  directions, and  $\xi$  is the phase constant to be determined.

Now we obtain wave fields generated by the analytical solution and by the numerical model. The wave to be generated has a period of  $T = 1$  s and an amplitude of  $a_0 = 4$  cm, with propagation direction as the  $x$  axis. The domain is shown in Fig. 10. The dimension of the domain is  $L_x = L_y = 20$  m and the water depth is constant across the domain with  $h = 0.45$  m. To demonstrate the effect of wave diffraction, we choose a small source region whose center source line is located from point ( $x = 2$  m,  $y = y_1 = 5$  m) to point ( $x = 2$  m,  $y = y_2 = 15$  m). The width of the source region  $W = |x_2 - x_1|$  is about 0.45 m.

The analytical solution for the wave field at an instance is obtained by taking the real part (or the imaginary part) of  $\eta(x, y)$  from Eq. (5). Wave amplitude is obtained by taking the module of  $\eta(x, y)$ . The constant  $A$  is determined by the condition that the averaged wave amplitude along the domain center line in  $x$  axis is equal to the desired

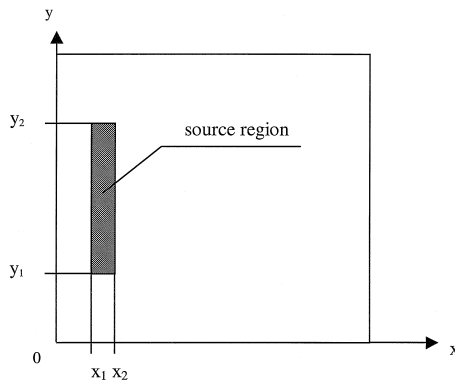


Fig. 10. Computational domain for comparison between the analytical solution and the model.

wave amplitude. Fig. 11(a) shows the analytical solution of surface elevation, with the phase constant specified as  $\xi = -\pi/2$  (so that both phases of analytical solution and the numerical model are the same). The snapshot of surface elevation generated by the numerical model at  $t = 60$  s is shown in Fig. 11(b). Both wave fields are quite similar. Strong diffraction effect can be seen around the two ends of the center source line where the source function amplitude drops abruptly to zero from a constant value.

Numerical integration is required to obtain the analytical solution defined in Eq. (55). The grid sizes for the numerical integration are chosen to be the same as those used in the numerical model, which are  $\Delta x = 0.05$  m and  $\Delta y = 0.1$  m. The same  $\beta$  value is used in both cases, i.e.,  $\beta = 36.3 \text{ m}^{-2}$ .

The snapshot shown in Fig. 11(b) is obtained by running the model for sufficiently long and a steady state wave field is reached. To reduce the effect of reflection due to limited domain size, 2 m wide sponge layers are added to all four sides. Therefore, the

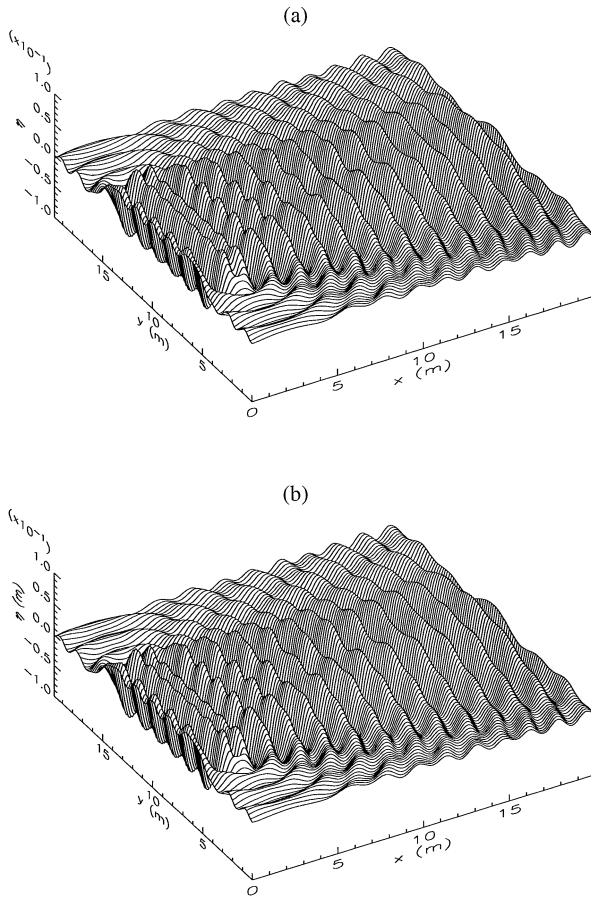


Fig. 11. Comparison of 2D wave fields: (a) analytical solution; (b) numerical model.

actual computational domain for the model is 24 m by 24 m, though a domain size of 20 m by 20 m is shown in Fig. 11(b). The time step for the model is chosen to be  $\Delta t = 0.01$  s. The governing equations for the model is the linearized form of Nwogu’s extended Boussinesq equations.

To better quantify the comparison, five cross-sections along  $x$  axis are made for the wave fields generated by the model and by the analytical solution. Fig. 12 shows the comparison of the cross-sections. Except for the source region center at  $x = 2$  m, there is little difference for the surface elevations between the model results and the analytical solution. The model is proved to be capable of generating the correct wave field.

Due to extremely short source region, the diffraction effect shown in Fig. 11 is quite large and the resulting wave field is not acceptable. In order for the model to generate a reasonable wave field, we need to increase the length of the source region. In the actual model application, the length of the source region is taken to be the same as  $L_y$ , the domain dimension in  $y$  axis. To evaluate the effect of source region length on the uniformity of the wave field, we run the model with different values of  $L_y$  to generate the same desired wave as shown in Fig. 11 (i.e., wave period  $T = 1.0$  s, wave amplitude  $\eta_0 = 4$  cm and wave direction  $\theta = 0^\circ$ ). Along the domain center line in  $x$  direction (i.e., at  $y = L_y/2$ ), time series data of surface elevation are collected and the corresponding wave heights are obtained. Fig. 13 shows the comparison of wave height variation for different domain sizes. As expected, the diffraction effect to the wave field in the center region decreases as the domain size in  $y$  direction increases.

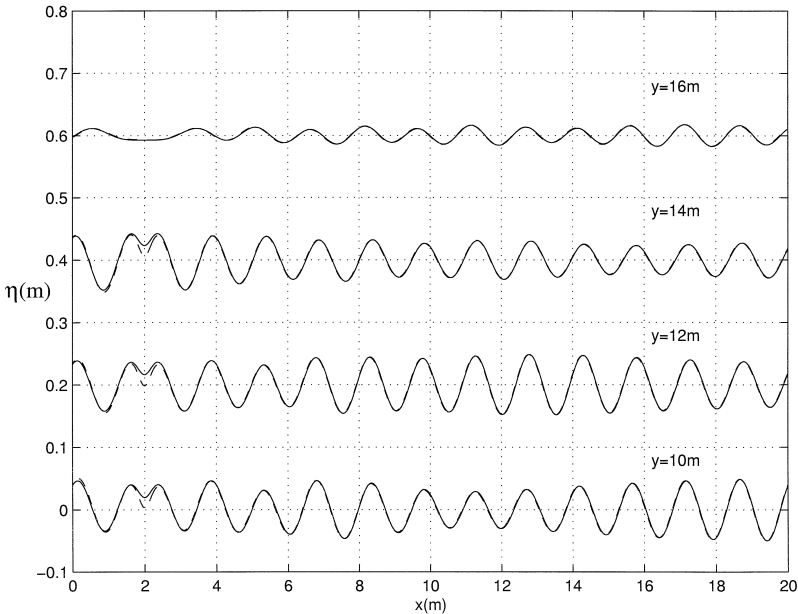


Fig. 12. Comparison of surface elevation between the model (dashed line) and the analytical solution (solid line).

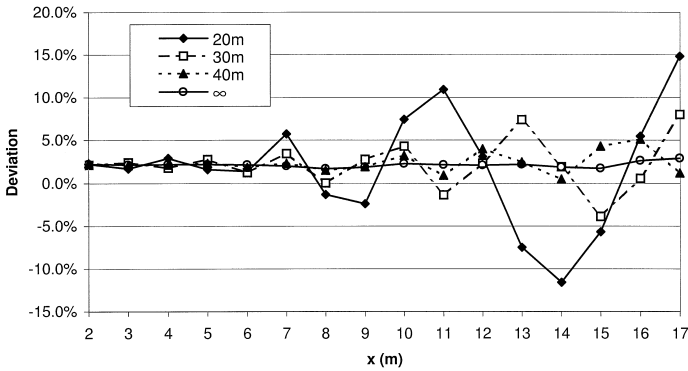


Fig. 13. Wave height variation from the model for different source lengths.

The diffraction effect also depends on the treatment of the side boundaries. If we use reflecting boundary conditions on the side, then there will be infinite number of the mirror image for the source region, making the effective source region length infinite. If we use sponge layers on the sides, the source region will be effectively cut off to a finite length, with maximum value to be  $L_y$ , the domain size in  $y$  axis. The diffraction effect will affect the uniformity of the generated wave field. For the case of zero incident wave angle in a flat bathymetry, we can use the model with finite domain size  $L_y$  to generate a wave field without diffraction effect. The wave height variation in Fig. 13 corresponding to this case is shown by  $L_y = \infty$ . The slightly higher value of wave height with  $L_y = \infty$  may be due to the small reflection effect from sponge layers on both left and right ends of the domain. Increasing the sponge layer size will decrease the discrepancy.

### 3.3.2. Comparison to experiment

To illustrate the importance of wave refraction and diffraction effect over complex bathymetry, Berkhoff et al. (1982) conducted a laboratory study of 2D monochromatic wave propagation over a plane beach with an elliptic shoal. The experiment layout and the transects for collecting wave data are shown schematically in Fig. 14. Monochromatic wave with period  $T = 1$  s and amplitude  $\eta_0 = 2.32$  cm is generated by a wavemaker at  $y = -10$  m. The bottom bathymetry consists of an elliptic shoal resting on a plane beach with a constant slope of  $1/50$ . The bottom contours on the slope are oriented at an angle of  $20^\circ$ . Detailed formula for the bottom bathymetry can be found in (Berkhoff et al., 1982).

Due to the relatively large  $kh$  value ( $kh = 1.9$  in the region of the wavemaker), standard Boussinesq equations of Peregrine (1967) are not valid for the simulation. However, the extended Boussinesq equations of Nwogu (1993) can be applied to this case, as shown by Wei and Kirby (1995). The wavemaker boundary condition used in (Wei and Kirby, 1995) is based on a conventional method, i.e., by combining specified incident wave condition with radiation condition. The simulation had to be terminated at about  $t = 35$  s when large reflected waves reached the wavemaker boundary, which affects the accuracy of the model.

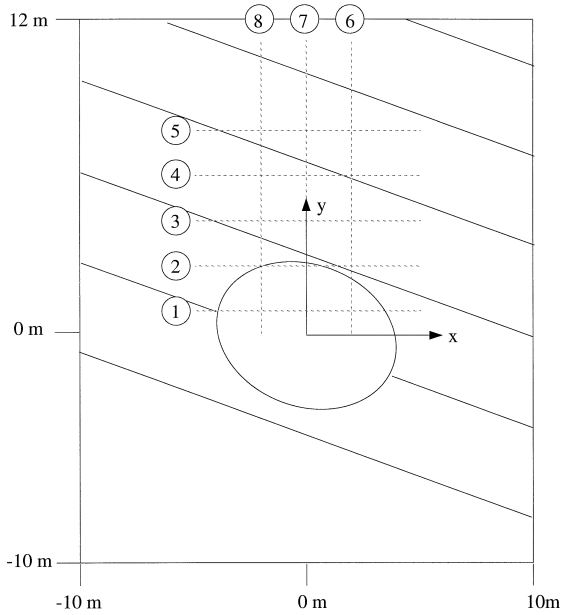


Fig. 14. Bottom geometry of the experiment of Berkhoff et al. (1982).

By using the source function method, the reflected waves reaching the wavemaker boundary are effectively dissipated by the sponge layer behind the source region. We run the model with the source function method to  $t = 50$  s without any stability problems. The grid sizes used in the model are  $\Delta y = 0.05$  m (in the direction of wave propagation), and  $\Delta x = 0.1$  m, and the time step is  $\Delta t = 0.01$  s. Sponge layers of 3 m wide are placed behind the source region and on the far end of the domain. Totally reflecting walls are placed on the two side boundaries, which is equivalent to having infinite length of source region.

Fig. 15 shows the comparison of wave amplitude along all the eight transects between the experimental data and the model results. The wave amplitude for the model is obtained by averaging those of the last four wave periods of simulation (i.e., from  $t = 46$  s to  $t = 50$  s). The agreement between data and model is excellent. These results are also presented in (Kirby, 1997). Compared to the results shown in (Wei and Kirby, 1995) based on traditional method, the accuracy obtained using the source function method increases significantly.

The model results shown in Fig. 15 are based on the extended Boussinesq equations derived by Nwogu (1993). We also run the model based on the fully nonlinear Boussinesq model of Wei et al. (1995), with the same model parameters. Though nonlinearity is very important for the example (Kirby and Dalrymple, 1984), there is little difference between the results based on these two sets of equations. We conclude that nonlinearity is not strong enough to distinguish the weakly and strong nonlinear effects.

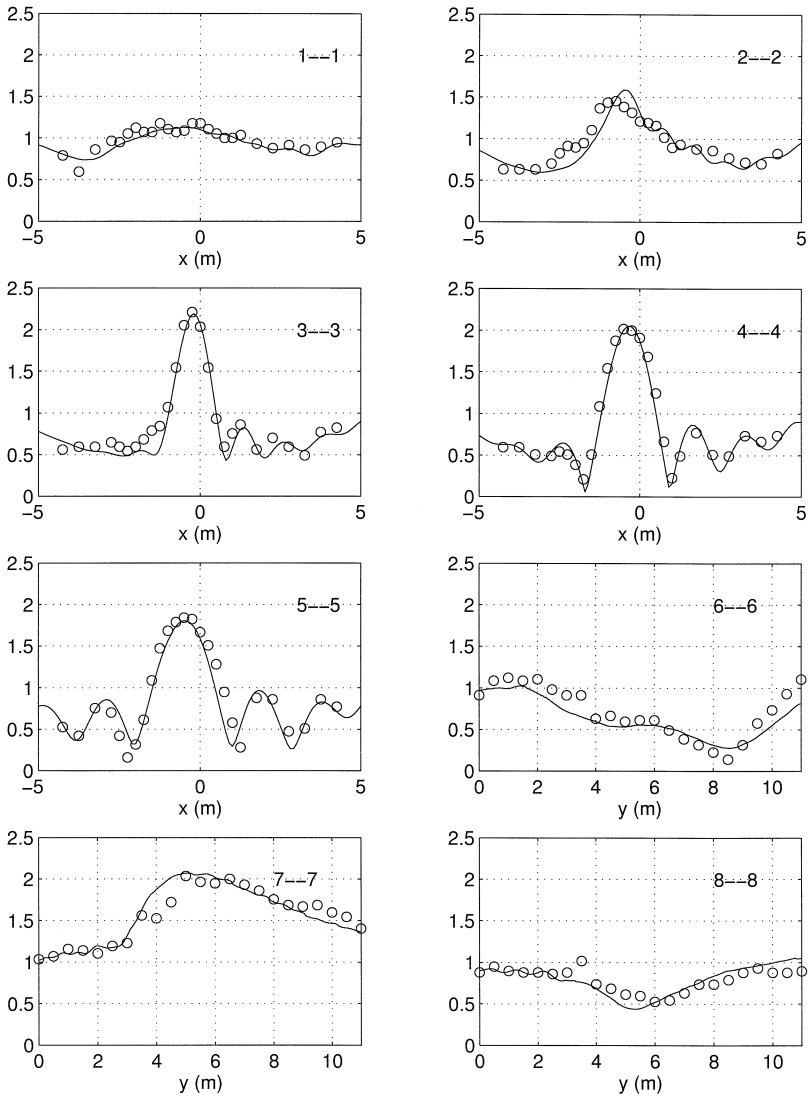


Fig. 15. Wave height comparison between model (————) and data (◦ ◦ ◦) along different transects for the experiment of Berkhoff et al. (1982).

### 3.4. 2D random wave

Similar to the case of 1D random wave, we can generate time series of the source function along the source line  $F(y, t)$  from the time series of surface elevation along that line  $\eta(y, t)$ . These two functions are defined as

$$\eta(y, t) = \frac{1}{4\pi^2} \int \int \eta_0(\lambda, \omega) \exp[i(\lambda y - \omega t)] d\omega d\lambda \tag{57}$$

$$F(y, t) = \frac{1}{4\pi^2} \int \int D(\lambda, \omega) \exp[i(\lambda y - \omega t)] d\omega d\lambda \quad (58)$$

where relation between  $\eta_0(\lambda, \omega)$  and  $D(\lambda, \omega)$  is defined by Eq. (36). In practice, however, it is not possible to provide the required time series of surface elevation for every grid point along the source line. Therefore, the time series of source function along the source line  $F(y, t)$  in the model is mostly generated by a given input wave spectrum.

Two methods can be applied to obtain the corresponding time series of source function  $F(y, t)$ . The first method is to use 2D FFT method. Given the wave spectrum (including the frequency spectrum and the direction spectrum), the amplitude of the surface elevation  $(\eta_0)_{i,j}$  corresponding to frequency  $\omega_i$  and  $y$  direction wavenumber  $\lambda_j$  is first obtained. The corresponding amplitude of the source function  $D_{i,j}$  for each component is then determined from Eq. (36). Adding random phase to each component gives the complex Fourier coefficient for the source function  $F(y, t)$ . Applying inverse FFT to the complex Fourier coefficients, the time series of source function  $F(y, t)$  is then determined.

The second method is direct computation. By dividing the 2D wave spectrum into  $N$  components in the frequency domain and  $M$  components in the directional domain, we first obtain the amplitude of surface elevation  $(\eta_0)_{i,j}$  for each wave component with frequency  $\omega_i$  and direction angle  $\theta_j$  (or wavenumber in  $y$ -axis  $\lambda_{i,j} = k_i \sin \theta_j$ ). The corresponding amplitude of source function  $D_{i,j}$  is then obtained from Eq. (36). Then the time series of source function for the random wave is given by

$$F(y, t) = \sum_{i=1}^N \sum_{j=1}^M D_{i,j} \cos(\omega_i t - k_i \cos(\theta_j) y + \xi_{i,j}) \quad (59)$$

where  $\xi_{i,j}$  is random phase whose value is in the range of  $(0, 2\pi)$ .

Fig. 16 shows a snapshot of random wave field at  $t = 200$  s generated by direct method on a flat bottom with depth  $h = 0.45$  m. The numbers of grid points are  $m_x = 201$  and  $m_y = 401$ , grid sizes are  $\Delta x = \Delta y = 0.1$  m, and time step  $\Delta t = 0.01$  s. The input random wave is based on the same TMA spectrum as that in the experiment of Vincent and Briggs (1988) for case  $N1$ , with peak wave period  $T_p = 1.3$  s, input significant wave height  $H_s = 7.75$  cm, frequency distribution parameter  $\gamma = 2$ , and directional spreading parameter  $\sigma_m = 10^\circ$ . We use direct method in the model to generate the time series of source function. The number of frequency components is  $N = 80$  and the number of directional components is  $M = 40$ . The spectra are divided such that the energy for each component is approximately the same. The source region for the model is located at  $x = 2$  m and from  $y = 0$  m to  $y = 40$  m.

Though the wave field shown in Fig. 16 looks quite random, the majority of the waves are traveling in the  $x$  direction, as evident by the wave crest lines which are approximately in  $y$  direction. This result is consistent with the input parameter in the model for narrow directional spreading ( $\sigma_m = 10^\circ$ ). To evaluate the model quantitatively, we run the model for sufficiently long (to 400 s) and record the time series data of surface elevation at selected locations, from which we compute statistical properties of the random wave field. Due to zero initial condition used in the model, the first 20 s

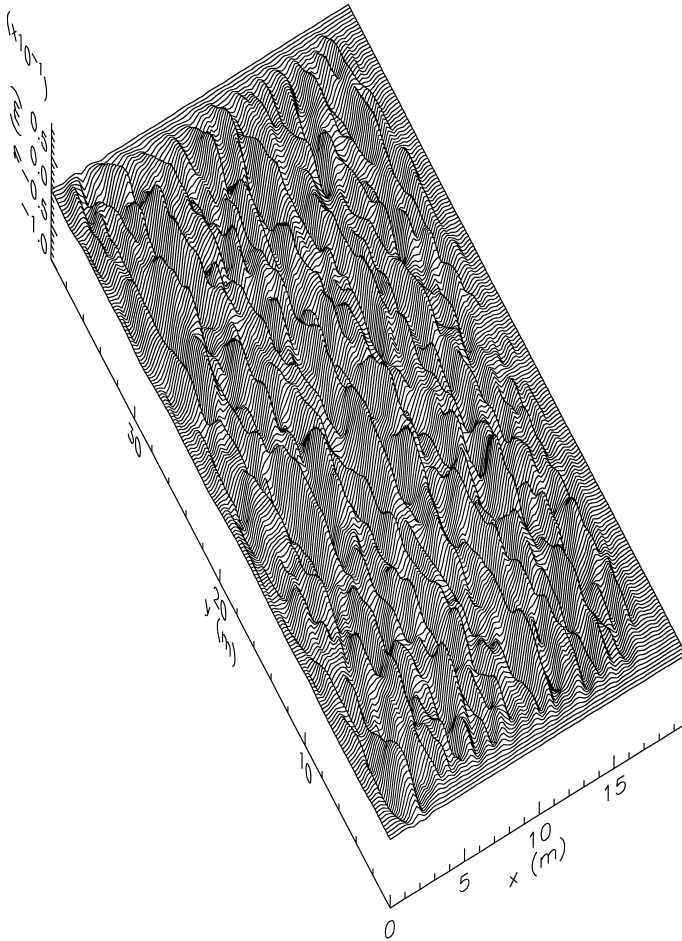


Fig. 16. Snapshot of 2D random wave field at  $t = 200$  s generated by the model.

of data is discarded for statistical computation. The time step for the collected time series of data is  $\Delta t = 0.02$  s. Using zero upcrossing method, we obtain the corresponding significant wave heights. Table 1 shows the results of wave heights and the coordinates of these 20 gauge locations.

Table 1  
Distribution of significant wave height (in cm)

	$x = 3$ m	$x = 5$ m	$x = 7$ m	$x = 10$ m
$y = 15$ m	7.20	6.93	6.79	6.74
$y = 18$ m	7.60	7.54	7.41	7.29
$y = 20$ m	7.43	7.56	7.70	7.68
$y = 22$ m	6.89	6.78	6.75	6.74
$y = 25$ m	6.71	6.80	6.92	7.34

The significant wave heights shown in Table 1 exhibit deviations for different gauges. These deviations are expected for any statistical properties from a random wave field. The normalized standard deviation of the significant wave heights for all 20 gauges is  $\sigma = 5.14\%$ . If we run the model for longer simulation and collect more time series of data, the deviation of statistical properties between different points will be reduced. The averaged value of the significant wave heights for all 20 gauge is 7.14 cm, which is about 8% smaller than the input value of  $H_s = 7.75$  cm. To investigate this problem, we obtain 20 sets of the time series of surface elevation along the source line

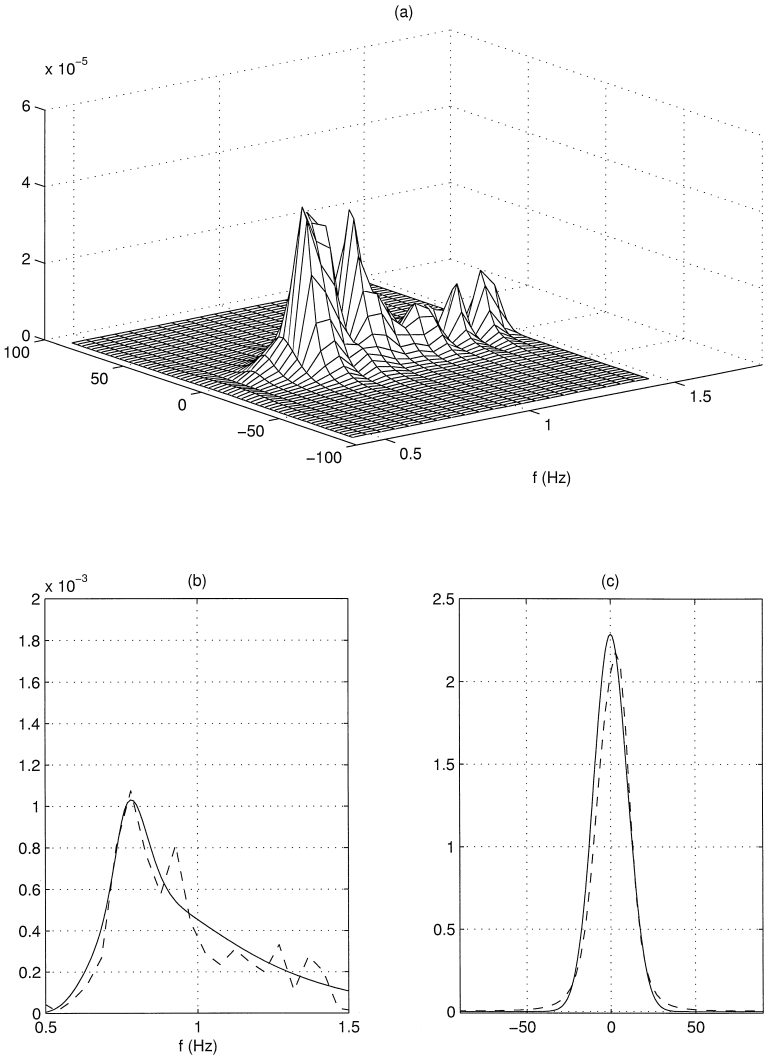


Fig. 17. (a) Computed 2D spectrum; (b) frequency spectrum; (c) directional spectrum for peak frequency. In (b) and (c), solid line is the input spectrum and dashed line is the computed spectrum.

directly from the input spectrum. The mean value of the significant wave heights for these 20 sets is 7.28 cm, which is also smaller than the input value. We notice that the difference between the significant wave height obtained from spectrum and that obtained from time series data is the major factor for this discrepancy between the input value and those in Table 1. Other factors may also contribute to this discrepancy. These factors include the diffraction effect due to the finite length of source region, the dissipation due to absorbing boundary condition on the sides, and the dissipation by applying numerical filter in the model.

To further examine the generated wave field, we compute the corresponding 2D spectrum and compare the averaged frequency spectrum and the directional spectrum at the peak frequency to the input spectrum, as shown in Fig. 17. The maximum likelihood method (MLM) is used to evaluate the spectrum from the time series of surface elevation surface elevations at four gauge locations. The coordinates of the gauges are  $x = 4$  m and  $y = (19$  m, 19.5 m, 20 m, 20.5 m). In spectrum computation, the time series data at each location is divided into 18 segments, each of which consists of 1024 points of data, with  $\Delta t = 0.02$  s. FFT is performed to each segment of data and frequency spectrum in Fig. 17 is the averaged for all the segments in four gauges. The agreement between the input and computed spectrum is good, indicating that the model generates random waves with the desired spectrum.

#### 4. Tidal effects

In model applications where the source function method is combined with absorbing sponge layers to damp backward propagating and reflected wave energy, model boundaries may simply be specified as being closed. In this situation, tidal effects may be easily induced in the model by adding or subtracting mass through the source term in Eq. (8). (Note that this effect may not be obtained using the applied pressure distribution in Eq. (37), as the response to a steady or quasi-steady pressure forcing would simply be an inverse-barometer distortion to the surface in the region of the source.) In this case, we establish a characteristic time scale for the model as  $L_m/c_0$ , where  $L_m$  is the horizontal scale of the model and  $c_0$  is a characteristic long wave speed for the model. For any physical process which adds or drains mass from the model domain, and which has a characteristic time scale  $T_0$  which is large compared to the model characteristic time scale, it may be assumed that the surface elevation changes uniformly in response to the added or subtracted mass. Returning to Eq. (8), we may write the mass conservation equation as

$$\eta_t + \nabla \cdot \mathbf{M} = F(\mathbf{x})s(t) \quad (60)$$

where  $\mathbf{M}$  is the mass flux vector and  $\mathbf{x}$  is vector position. Denoting the model domain by  $\Omega$  and its boundary by  $\partial\Omega$ , we integrate Eq. (60) over  $\Omega$  and apply the divergence theorem to obtain

$$\frac{d}{dt} \int_{\Omega} \eta d\mathbf{x} + \int_{\partial\Omega} \mathbf{M} \cdot \mathbf{n} dl = \int \int_{\Omega} F(\mathbf{x}) d\mathbf{x} s(t). \quad (61)$$

For long timescale motions where we can assume that  $\eta$  is effectively uniform over  $\Omega$ , we denote the area of  $\Omega$  by  $\mathcal{A}$  and obtain

$$\mathcal{A} \frac{d\eta}{dt} + \int_{\partial\Omega} \mathbf{M} \cdot \mathbf{n} dl = \int \int_{\Omega} F(\mathbf{x}) d\mathbf{x} s(t). \quad (62)$$

Changes in mean water level in the model can obviously be induced either by mass flux across model boundaries (expressed by the line integral) or addition of mass through the source (expressed by the RHS of the two preceding equations). Neglecting the first effect, we obtain the control signal  $s(t)$  as

$$s(t) = \frac{\mathcal{A}}{\int \int_{\Omega} F(\mathbf{x}) d\mathbf{x}} \frac{d\eta}{dt}. \quad (63)$$

The signal depends only on the rate of change of the surface, the area of the model, and the integrated volume of the source function distribution. For the Gaussian source function proposed above, we have

$$\int F(x) dx = \int_{-\infty}^{\infty} \exp(-\beta x^2) dx = \sqrt{\frac{\pi}{\beta}}. \quad (64)$$

## 5. Conclusions

We derived the theory for wave generation by internal source function for Boussinesq-type equations. Solutions to linearized governing equations are obtained using the Green's function method. The source function amplitude is related to the characteristics of the desired incident wave as well as to the width of source region. For random wave generation, the width of the source region is the same for all components of the wave to reduce the computation time.

We applied the model to study several cases of wave generation and propagation, including monochromatic waves and random waves, in both one and two dimensions. Model results are compared with experimental data for 1D random wave and for 2D monochromatic waves. The agreement between the data and model results is quite good. For 2D monochromatic wave with finite source length, we obtained the analytical solution to the Helmholtz equation. Good agreement between analytical solution and model result is found. We tested the model to generate a random wave in 2D with a given spectrum in a flat bottom domain. We obtained the time series of surface elevation at selected locations and computed the corresponding significant wave heights at these locations are obtained. We also computed the spectrum of the wave field based on Maximum Likelihood Method and compared with input spectrum. Model results indicate that the wave field generated by internal source function method is quite reasonable.

Diffraction effect becomes large if the length of the source line is small, or if the angle between the wave direction and the source line becomes small. To generate the desirable wave accurately in two dimension, large domain size in source line direction is required.

We are currently running the model to simulate 2D random wave propagation over complex bathymetry. Comparison between the model and data will be presented elsewhere.

## Acknowledgements

The work of James Kirby and Ge Wei was supported in part by the Army Research Office through University Research Initiative grant DAAL 03-92-G-0116. The work of Amar Sinha and Ge Wei was funded by the Army Research Office, Small Business Innovation Research (SBIR) program (contract no. DACA 39-97-C-0018). Amar Sinha and Ge Wei gratefully acknowledge the support and guidance of Dr. Zeki Demirebilek, US Army Waterways Experiment Station, Vicksburg, MS, the technical monitor of the SBIR project. We thank Kevin Haas (CACR, University of Delaware) for providing the Matlab program of analytical solution to Helmholtz equation, and thank James Kaihatu (NRL, Stennis Space Center) and Jane Smith (CERC, Waterways Experiment Station) for their permission to use their Fortran program to compute 2D spectrum based on the Maximum Likelihood Method.

## References

- Berkhoff, J.C.W., Booy, N., Radder, A.C., 1982. Verification of numerical wave propagation models for simple harmonic linear water waves. *Coastal Eng.* 6, 255–279.
- Engquist, B., Majda, A., 1977. Absorbing boundary conditions for the numerical simulation of waves. *Math. Comp.* 31, 629–665.
- Greenberg, M., 1971. *Application of Green's Functions in Science and Engineering*. Prentice-Hall, Englewood Cliffs, NJ, 141 pp.
- Israeli, M., Orszag, S.A., 1981. Approximation of radiation boundary conditions. *J. Comp. Phys.* 41, 113–115.
- Kirby, J.T., 1997. Nonlinear, dispersive long waves in water of variable depth. In: Hunt, J.N. (Ed.), *Gravity Waves in Water of Variable Depth*. *Advances in Fluid Mechanics*, Vol. 10, pp. 55–125.
- Kirby, J.T., Dalrymple, R.A., 1984. A verification of a parabolic equation for propagation of weakly nonlinear waves. *Coastal Eng.* 8, 219–221.
- Larsen, J., Dancy, H., 1983. Open boundaries in short wave simulations—a new approach. *Coastal Eng.* 7, 285–297.
- Mase, H., Kirby, J.T., 1992. Hybrid frequency-domain KdV equation for random wave transformation. *Proc. 23rd Intl. Conf. Coast. Eng., Venice*, pp. 474–487.
- Nwogu, O., 1993. An alternative form of the Boussinesq equations for nearshore wave propagation. *J. Waterway, Port, Coast. and Ocean Eng.* 119, 618–638.
- Peregrine, D.H., 1967. Long waves on a beach. *J. Fluid Mech.* 27, 815–827.
- Vincent, C.L., Briggs, M.J., 1988. Refraction–diffraction of irregular waves over a shoal. *J. Waterway, Port, Coast. and Ocean Eng.* 115, 269–284.
- Wei, G., 1997. *Simulation of water waves by Boussinesq models*. PhD dissertation, University of Delaware, 202 pp.
- Wei, G., Kirby, J.T., 1995. Time-dependent numerical code for extended Boussinesq equations. *J. Waterway, Port, Coast. and Ocean Eng.* 121, 251–261.
- Wei, G., Kirby, J.T., Grilli, S.T., Subramanya, R., 1995. A fully nonlinear Boussinesq model for surface waves: Part 1. Highly nonlinear unsteady waves. *J. Fluid Mech.* 294, 71–92.